Journal of Solid State Chemistry 187 (2012) 249–257

Contents lists available at SciVerse ScienceDirect

Journal of Solid State Chemistry

journal homepage: www.elsevier.com/locate/jssc

Low-temperature synthesis, luminescence and phonon properties of Er and/or Dy doped $LaAlO_3$ nanopowders

Mirosław Mączka [a,*], Esmeralda Mendoza-Mendoza [b], Antonio F. Fuentes [b], Karol Lemański [a], Przemysław Dereń [a]

[a] Institute of Low Temperature and Structure Research, Polish Academy of Sciences, P.O. Box 1410, 50-950 Wrocław 2, Poland
[b] Cinvestav Unidad Saltillo, Apartado Postal 663, Saltillo, 25000 Coahuila, Mexico

ARTICLE INFO

Article history:
Received 20 December 2011
Received in revised form
12 January 2012
Accepted 15 January 2012
Available online 24 January 2012

Keywords:
Nanocrystallites
Perovskite
Infrared
Raman
Luminescence

ABSTRACT

$LaAlO_3$, $La_{0.9}Dy_{0.1}AlO_3$, $La_{0.9}Er_{0.1}AlO_3$ and $La_{0.8}Dy_{0.1}Er_{0.1}AlO_3$ nanocrystalline powders were synthesized in a two-step process by combining a mechanically induced metathesis reaction and molten salt synthesis. The proposed two-step methodology easily allows obtaining pure and/or doped perovskite-type $LaAlO_3$ nanopowders at remarkably low temperatures, i.e., already at 350 °C although firing at 500 °C is needed in order to get pure phases. The obtained samples were characterized by XRD, TEM, Raman, IR and luminescence methods. These methods showed that the mean crystallite size is near 50–60 nm and the $LaAlO_3$ nanocrystallites have $R\bar{3}c$ structure, the same as bulk $LaAlO_3$. Raman spectrum of nanocrystalline $LaAlO_3$ is very similar to that of bulk. In contrast to this behavior, IR spectra of the synthesized compounds are significantly different from the IR spectrum of bulk $LaAlO_3$. Origin of this behavior is discussed. Luminescence study showed that the cross-relaxation processes quench emission intensity of the samples doped with Dy^{3+} and Er^{3+}.

1. Introduction

Concentrated rare earth perovskites, $RAlO_3$, as well as $LaAlO_3$ doped with rare earth ions have attracted attention as potential laser materials [1–3]. In this context, $LaAlO_3$ doped with Er^{3+} or/and Dy^{3+} ions is of significant interest since the erbium doped materials are essential for long-distance optical communication systems and fabrication of eye safe laser [2,4] whereas the dysprosium doped materials have attracted much attention due to their white light emission [5]. $LaAlO_3$ is also a promising candidate for replacements of silica as a gate dielectric in ultra-high integration Si-based electronic devices [6].

$LaAlO_3$ perovskite has at room temperature a rhombohedral structure with $R\bar{3}c$ symmetry and it undergoes phase transition into the $Pm\bar{3}m$ cubic phase at T_c=800 K [7]. It is well known that physical and chemical properties of materials are significantly modified when size of crystallites is of order of nanometers. Moreover, the technology of preparation also influences the physical properties of nanosized materials. Therefore, many attempts have been undertaken to synthesize pure and rare earth doped nanocrystalline $LaAlO_3$ in order to compare their properties with those of bulk samples. These materials were synthesized by various methods such as co-precipitation [8–10], a citrate-precursor [11,12], ethylenediaminotetraacetic acid precursor [13], emulsion combustion [14], polyvinyl alcohol evaporation [15], mechanochemical alloying [16] and molten salt methods [17,18]. It has been shown that in case of molten salt method the synthesis temperature could be lowered to 630 °C but the obtained crystallites were of the order of micrometers [16]. In the mechanochemical synthesis smaller crystallites could be obtained but this method suffers from a very limited production capacity and is not suitable for synthesis of small nanocrystallites of $LaAlO_3$. Other mentioned above methods require heat-treatment in order to obtain nanocrystalline samples. Up to now, the lowest crystallization temperature (600 °C) was achieved using a co-precipitation technique followed by gelation and removal of chloride ions [10]. It is worth to add that Deren et al. showed by Raman spectra, XRD as well as monitoring the R line of Cr^{3+} emission that diminishing of the crystallite size of $LaAlO_3$:Pr^{3+} stabilizes at room temperature the $Pm\bar{3}m$ structure [8,19]. In contrast to this conclusion, the diffraction pattern of $LaAlO_3$:Tb^{3+} and pure $LaAlO_3$ with the average crystallite size of 20 and 60 nm, respectively, was assigned to the $R\bar{3}c$ structure [9,14].

The present paper reports synthesis of nanocrystalline $LaAlO_3$, $La_{0.9}Dy_{0.1}AlO_3$, $La_{0.9}Er_{0.1}AlO_3$ and $La_{0.8}Dy_{0.1}Er_{0.1}AlO_3$ using a novel two-step process, which combines a mechanically induced metathesis reaction and molten salt synthesis. We will show that this method allows obtaining nanocrystallites of the target

* Corresponding author. Fax: +48 71 3441029
E-mail address: m.maczka@int.pan.wroc.pl (M. Mączka).

0022-4596/$ - see front matter © 2012 Elsevier Inc. All rights reserved.
doi:10.1016/j.jssc.2012.01.028

perovskites already at 350 °C although firing at 500 °C is needed in order to get pure phases. The synthesized materials have been characterized by XRD, TEM, Raman, IR and electronic spectroscopy. The obtained results are compared with those obtained for bulk $LaAlO_3$ and previously reported nanocrystalline $LaAlO_3$ in order to obtain information how properties of this perovskite change with decreasing particle size and the technology of preparation.

2. Experimental

Pristine and Er^{3+} and/or Dy^{3+} doped $LaAlO_3$ powders ($Er_{0.1}La_{0.9}AlO_3$, $Er_{0.1}Dy_{0.1}La_{0.8}AlO_3$ and $Dy_{0.1}La_{0.9}AlO_3$) were prepared by a novel two-step method consisting of a mechanically induced metathesis reaction and short firing at low temperatures. First, analytical grade hydrated metal nitrates ($Al(NO_3)_3 \cdot 9H_2O$, $Er(NO_3)_3 \cdot 5H_2O$, $La(NO_3)_3 \cdot 6H_2O$ and $Dy(NO_3)_3 \cdot 5H_2O$) were weighed out as required by stoichiometry, mixed with the appropriate amount of NaOH and dry milled together for 30 min in a planetary ball mill using 125 ml volume yttria partially stabilized zirconia (5.2 wt% Y_2O_3) containers and balls (20 mm diameter; balls-to-powder mass ratio = 10:1) and a rotating disk speed of 350 rpm. The amount of reactants was salt-balanced such that there was no alkali metal or nitrates excess (total metal nitrates/sodium hydroxide molar ratio equal to 1:3). The resulting activated precursor material was dried for 1 h at 120 °C to reduce moisture and minimize violent gas evolution on melting, and then mixed with $NaNO_2$ (NaOH:$NaNO_2$ molar ratio = 3:1), homogenized and finally loaded into alumina crucibles to promote the formation of the target material. The as-obtained $LaAlO_3$ precursor materials were fired for 3 h in air either at 350 or 500 °C using an electrical furnace (heating rate = 5 °C min^{-1}) and cooled thereafter to room temperature. After running some preliminary tests, adding $NaNO_2$ and thus increasing oxygen ion concentration and reactivity of the melt, was found necessary in order to obtain single phase samples. Furthermore, $NaNO_2$ decreases substantially $NaNO_3$ melting point to a lowest temperature of ~230 °C for the 1:1 mole ratio composition versus 301 °C for the pure nitrate [20].

Solidified melts obtained after firing were washed with distilled water to remove the soluble fraction ($NaNO_3$ byproduct and added $NaNO_2$) whereas the solid residue was collected by centrifugation and/or filtration. This step was repeated a few times until no traces of NO_3^- or NO_2^- ions were detected by FTIR spectroscopy. Phase identification at different stages of the process was carried out by using X-ray powder diffraction in a Philips X'Pert diffractometer with Ni-filtered Cu-K_α radiation (λ=1.5418 Å). In addition, the thermal behavior of the precursor material obtained after milling was examined by simultaneously recording the thermogravimetric and differential thermal analysis curves in a Perkin-Elmer Pyris Diamond TG/DTA instrument using a typical sample size of 15 mg, a 5 °C/min heating rate and an air static atmosphere.

Further XRD characterization was carried out at room temperature by using X'Pert PRO powder diffractometer (PANalytical, The Netherlands) working in the transmission or reflection geometry, equipped with a linear PIXcel detector and using Cu-$K_{\alpha 1}$ radiation (λ=1.54056 Å) in the 2Θ range from 5° to 140° with a step of 0.026°.

The particle size and morphology of the obtained samples were performed using a Philips CM20 SuperTwin transmission electron microscope (TEM) providing 0.24 nm resolution. Specimens for TEM were prepared by grinding the samples in mortar and dispersing in methanol with ultrasonic agitation. A droplet of suspension was deposited on a microscope grid covered with carbon film.

Infrared spectra were measured with a Biorad 575C FT-IR spectrometer in KBr pellet for the 4000–400 cm^{-1} region and in Nujol suspension for the 500–50 cm^{-1} region. The Raman spectra were measured with the Jobin-Yvon Ramanor U-1000 spectrometer equipped with the photomultiplier photon counting electronic system. The 514.5 nm line of the Ar^+ laser (power of ca. 200 mW) was used as the excitation source. Both IR and Raman spectra were recorded with a spectral resolution of 2 cm^{-1}.

The emission spectra were recorded using a Jobin Yvon THR1000 monochromator with CCD camera. As the excitation sources we used argon laser with the 458 and 488 nm line and a Ti: sapphire laser with the UV line at 355 nm.

3. Results and discussion

3.1. Synthesis, thermal analysis and X-ray powder diffraction

Molten salt synthesis (MSS) of multicomponent oxides is normally carried out by blending the appropriate inorganic precursor salts with an excess of the desired flux and firing the mixture at the reaction temperature, above the flux melting point. Most commonly fluxes used in MSS include alkali and alkaline-earth metal hydroxides, nitrates, halides, carbonates, or sulphates; inexpensive nitrates and/or their eutectic mixtures are normally preferred because of their lower melting points (> 350 °C), stability over a wide liquid temperature window (typically up to ~550–600 °C) and high water solubility which facilitates recovering of the target phase by simply washing the solidified melt with distilled water. However, preliminary attempts carried out in our group to produce $LaAlO_3$ powders by mixing hydrated La^{3+} and Al^{3+} nitrates with commercially available sodium nitrate and firing the reaction batch above $NaNO_3$ melting point (301 °C), were unsuccessful. In fact, $LaAlO_3$ powders have been previously obtained in molten salts only by using complex fluxes of high melting points (> 600 °C) such as KF/KCl or alkali metal carbonate eutectics, as reaction media [17,18]. Even in these cases and because of their low mutual reactivity and La^{3+} sensitivity towards atmospheric CO_2 and moisture, the obtained target material was mixed with unreacted oxides, lanthanum carbonates and oxycarbonates, which made necessary introducing a final purification step using concentrated HCl or even using an inert nitrogen atmosphere, to get single phase products. As it will be shown here, using first a metathesis reaction fulfills two goals: on the one hand to generate in-situ sodium nitrate, high-lattice energy byproduct and thus the driving force behind the displacement reaction itself and at the same time, the main flux for the second step; on the other hand and more important, to circumvent La^{3+} and Al^{3+} low reactivity in molten nitrates by producing a suitable precursor material for the synthesis of $LaAlO_3$ powders at low temperatures. A similar procedure has been already successfully used in this group for the synthesis of another interesting ceramic material, Bi_2WO_6 [21]. In order to illustrate the synthesis procedure, the dysprosium singly-doped $LaAlO_3$ sample ($Dy_{0.1}La_{0.9}AlO_3$) would be used as representative of the series on the understanding that similar results were obtained for the remaining three samples prepared in this work.

Fig. 1(a) shows the XRD pattern of the Dy, Al and La hydrated nitrates mixture together with NaOH after milling and adding the $NaNO_2$ powders as described in the Experimental section. To ease the discussion, the characteristic reflections of rhombohedral $NaNO_3$ (ICDD PDF card no. 36-1474) and orthorhombic $NaNO_2$ (ICDD PDF card no. 06-0392) are also shown at the bottom and

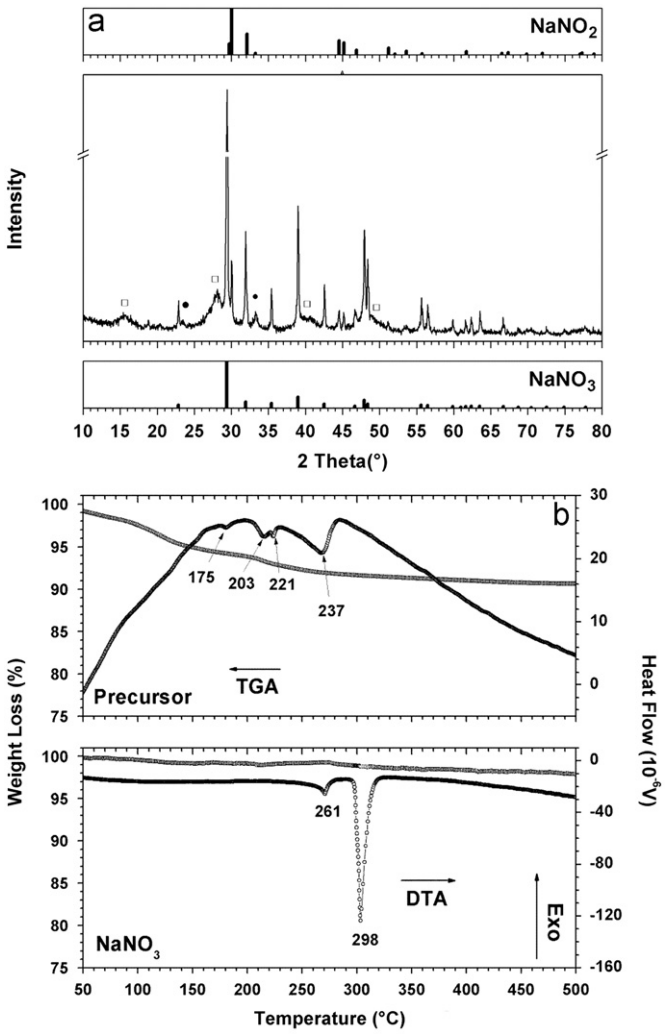

Fig. 1. (a) XRD pattern obtained after milling the reaction mixture for 30 min as described in the Experimental section. Top and bottom patterns show the characteristic reflections of $NaNO_2$ and $NaNO_3$, respectively. Empty squares and solid circles show some characteristic reflections of $La(OH)_3$ and $LaAlO_3$, respectively also formed on milling. (b) Thermal analysis curves obtained for our milled precursor material (top) and pure $NaNO_3$ (bottom).

top respectively of this figure. The first conclusion to be drawn from this XRD pattern is that indeed, a metathesis or displacement reaction took place on milling as proved by the presence of the characteristic reflections of $NaNO_3$ in the sample: e.g., Miller indexes (1 0 4), (0 0 6), (1 1 3) and (0 1 8) at 29.40° (100% relative intensity), 31.89°, 38.96° and 47.95° (2θ), respectively. The other crystalline phase clearly identified in this XRD pattern is added $NaNO_2$ denoted by reflections showing at $2\theta=30.03°$ (Miller indexes (1 0 1); 100% relative intensity), 32.09° (0 2 0), 44.52° (1 2 1) and 45.18° (1 1 2). As expected then, such a short milling time was enough for the sodium ions to replace the trivalent cations in their nitrates and transform them into different chemical species, which incidentally are difficult to identify by XRD because of lacking of long-range atomic ordering and thus being amorphous to X-ray diffraction. However, Fig. 1(a) does suggest La^{3+} being at least partially present as very fine or poorly crystalline hexagonal $La(OH)_3$ as denoted by a series of broad and very low intensity reflections centered around ~16°, ~28°, ~40° and ~48° (2θ) (ICDD PDF card no. 36-1481), which were identified as the (1 0 0), (1 1 0) and (1 0 1) [100% relative intensity], (2 0 1), (3 0 0) and (2 1 1) set of reflections, respectively. Interestingly, two low intensity peaks found at 23.4° and 33.4° (2θ) were identified as the (0 1 2) and (1 1 0) reflections of rhombohedral $LaAlO_3$ (ICDD PDF card no. 31-0022) revealing that a small amount of the target perovskite-type phase is even formed through a true mechanochemical reaction after such short milling. As mentioned before, $LaAlO_3$ has been previously prepared by using high-energy mechanical milling but only using transient alumina as Al-source, i.e, aluminum oxide obtained after firing between 400 and 800 °C for 2 h the corresponding hydroxide $Al(OH)_3$ whereas no reaction was observed when using corundum type Al_2O_3 [16].

Fig. 1(b) shows the thermal analysis curves characteristic of the same Dy-containing precursor material (top) together with those of commercially available $NaNO_3$ (bottom) for comparison, when both were subjected to the same heating/cooling program. Whereas only two endothermic events and minimal weigh losses are observed in the latter, the reaction of the former to increasing temperature is more complex. Thus, both endothermic events without associated weight losses found at 261 and 298 °C in the $NaNO_3$ DTA curve are assigned to a reversible polymorphic transformation from the room temperature and atmospheric pressure stable rhombohedral ordered form (form II) to a disordered $NaNO_3$ phase (form I) and subsequent melting, respectively [22]. The thermal analysis curves of our precursor material show below 500 °C at least four endothermic events at the following onset temperatures: 175, 203, 221 and 237 °C, and a total weight loss of ~8.4%. The $NaNO_3$–$NaNO_2$ binary phase diagram presents a single eutectic at the 1:1 mole fraction composition with a horizontal solidus at 230 °C ranging from 0.25 to 0.80 mole fraction of $NaNO_3$ and two subsolidus transitions close to 160 and 183 °C [20]. Much simpler are the thermal analysis curves of pure $NaNO_2$, which only show two endothermic events at 164 and 283 °C corresponding to a solid-state phase transition and melting, respectively. Therefore, the first endothermic event without associated weight loss observed in our case close to 175 °C is assigned to the second subsolidus polymorphic transformation mentioned above whereas the broad one with an onset temperature close to 237 °C also without associated weight loss, is thought to reflect the melting of the $NaNO_3$/$NaNO_2$ mixture. The remaining two events observed between 200 and 225 °C and associated to a small weight loss (~2%) are probably due to some dehydration process taking place on the precursor material on firing.

Based on these results, two reaction temperatures were selected for the molten salts step: 350 and 500 °C. Fig. 2 shows the XRD patterns of the same precursor material after firing 3 h at each of these temperatures; to ease the discussion we have also plotted in the same figure the characteristic reflections of both $NaNO_3$ (top) and $LaAlO_3$ (bottom). Interestingly, a new set of strong reflections is clearly evident in both cases besides those characteristic of the $NaNO_3$ byproduct and added $NaNO_2$, which were identified as belonging to perovskite-type $LaAlO_3$: e.g., rhombohedral $LaAlO_3$ most intense reflections of Miller indexes (1 1 0), (0 1 2), (2 0 2) and (0 2 4) at 33.41 (100% rel. intensity), 23.46, 41.20 and 47.98° (2θ), respectively (JCPDS-ICDD PDF card No. 31-0022). However, in the sample fired at 350 °C in addition to the target material, the presence of a small amount of hexagonal $La_2O_2CO_3$ (ICDD PDF card no. 37-0804) is also observed denoted by the presence of low intensity peaks at 25.2°, 25.9°, 27.7° and 30.4°, which were identified as its (1 0 0), (1 0 1), (1 0 2) and (1 0 3) [100% relative intensity] characteristic reflections. Increasing the firing temperature to 500 °C produces single-phase Dy-doped $LaAlO_3$ powders with no other crystalline compound present but $NaNO_3$ and $NaNO_2$. Therefore, these results do confirm that the metathesis reaction provided a suitable La and Al containing precursor material for the synthesis of perovskite-type $LaAlO_3$ in molten $NaNO_3$/$NaNO_2$ at remarkable low

temperatures. The same procedure was repeated for the remaining phases analyzed in this work with XRD patterns shown in Fig. 3: washing the as obtained powders with distilled water in every case rendered single phase pristine Er and/or Dy doped $LaAlO_3$ without requiring of any additional purification step as otherwise often needed when preparing ceramic materials by MSS. The XRD patterns show an evident shift towards lower angles (decreasing cell size) as the average size of the lanthanide ion (and thus the R_A/R_B ratio) in the A position of the ABO_3 perovskite decreases: $LaAlO_3$ (1.16 Å) > $Dy_{0.1}La_{0.9}AlO_3$ (1.147 Å) ≈ $Er_{0.1}La_{0.9}AlO_3$ (1.144 Å) > $Dy_{0.1}Er_{0.1}La_{0.8}AlO_3$ (1.131 Å). To calculate these values we have used the ionic radii given by Shannon [23] considering 8-coordinated cations because of insufficient data for 12-coordinated ions: La = 1.16 Å > Dy = 1.03 Å > Er = 1.00 Å.

Therefore, to this point we have shown that the proposed two-step methodology easily allows obtaining pure and/or doped perovskite-type $LaAlO_3$ nanopowders at remarkably low temperatures. Furthermore, this method compares favorably with existing techniques for the synthesis of $LaAlO_3$ powders: i.e., neither La^{3+} and Al^{3+} nitrates nor hydroxides allow obtaining this material as crystalline powders at such low temperatures as those described here. Hence, different attempts carried out to synthesize the target phase by first melting and then dehydrating and firing equimolar mixtures of both hydrated metal nitrates, have shown the onset of crystallinity of the product phase taking place typically in the 800–1000 °C range [24,25].

Fig. 3 shows that the experimental XRD patterns of the synthesized powders are very similar to the patterns of cubic or rhombohedral $LaAlO_3$ but the diffraction peaks are significantly broadened. This result shows that pure nanocrystalline phases of the target perovskites are formed at 500 °C. The question that arises is whether the crystal structure of the obtained nanosized crystallites is cubic or rhombohedral. The calculated XRD patterns for the cubic and rhombohedral phases show that due to symmetry lowering some of the diffraction lines should split and weak additional lines should appear at 2Θ near 39.4, 52.6, 63.8, 73.8, 83.5, 93.0, 102.5° etc. However, for the nanocrystalline samples this splitting and weak lines may be difficult to observe due to significant broadening of the diffraction lines. Fig. 4 shows enlarged part of the XRD pattern for $La_{0.9}Dy_{0.1}AlO_3$ together with the calculated XRD pattern for bulk $R\bar{3}c$ structure. As can be seen, this figure shows two features. First, the line near 2Θ= 89.6° is clearly asymmetric. This result indicates that it is composed of two components, as expected for the $R\bar{3}c$ structure. Second, some very weak lines are observed at 39.4, 52.6 and 73.8°, in agreement with additional weak lines expected for the $R\bar{3}c$ structure. Our present XRD results indicate, therefore, that the synthesized samples contain nanocrystallites of the $R\bar{3}c$ phase.

The particle size can be estimated from Scherrer's formula $D=K\lambda/\beta cos\Theta$, where D is the mean crystallite size along the (h k l) direction, λ is the X-ray wavelength (in our study λ = 1.54056 Å), β is broadening of the diffraction line (in radians), Θ is the angle

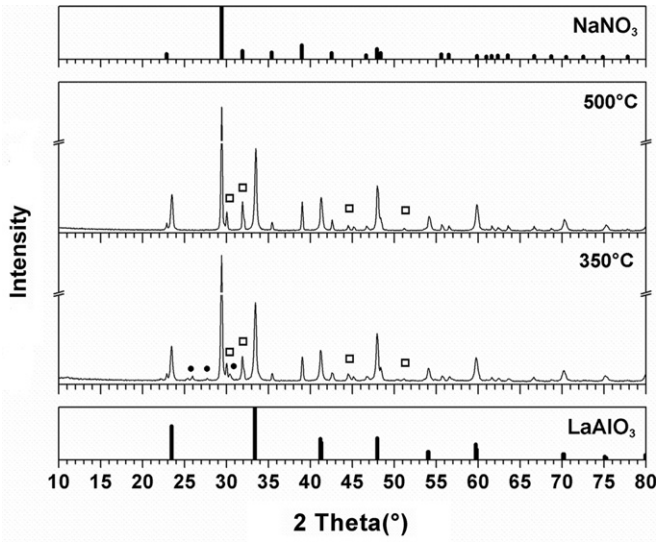

Fig. 2. XRD patterns obtained after firing the Dy containing precursor material for 3 h at 350 and 500 °C. Top and bottom patterns show the characteristic reflections of $NaNO_3$ and $LaAlO_3$, respectively. Empty squares in both patterns show some of the characteristic reflections of $NaNO_2$ whereas those labeled with a solid circle in the sample fired at 350 °C belong to $La_2O_2CO_3$.

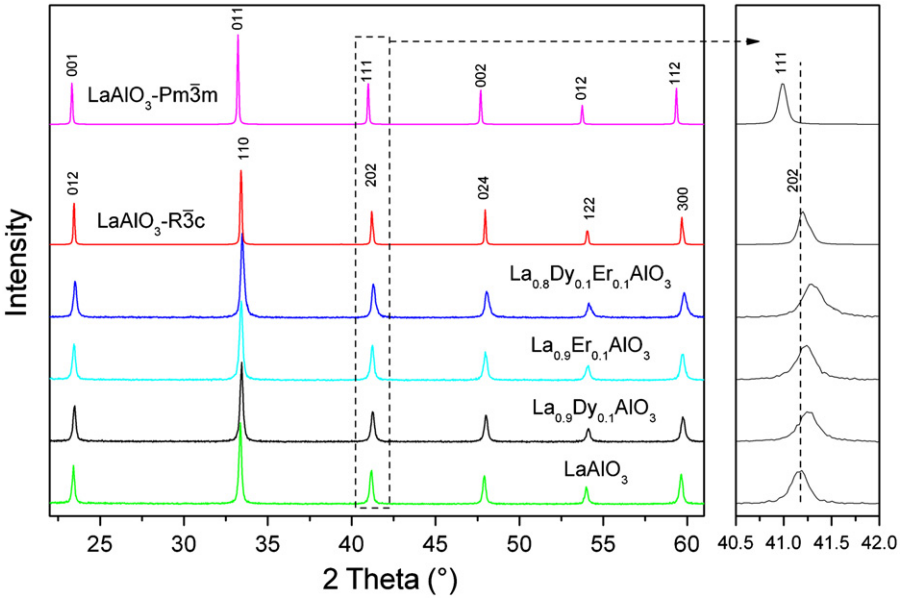

Fig. 3. XRD patterns of the four samples obtained in this work after firing at 500 °C and removing the water soluble fraction ($NaNO_2$ + $NaNO_3$) and enlargement of the area where the (2 0 2) reflection appears. The standard patterns of cubic and rhombohedral $LaAlO_3$ generated by powder diffraction diagram simulation program Poudrix V2 [26], using the published crystallographic data (ICSD files 90550 and 90534), are presented at the top.

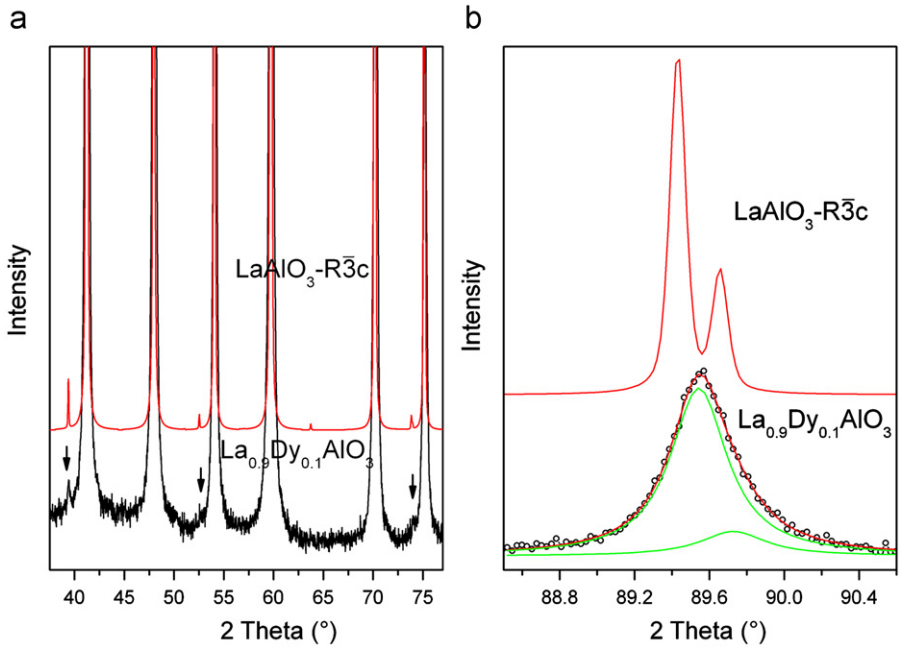

Fig. 4. (a) Enlarged part of XRD patterns of the nanocrystalline $La_{0.9}Dy_{0.1}AlO_3$ sample and the standard pattern of rhombohedral $LaAlO_3$ showing presence of weak lines (indicated by arrows). (b) Enlargement of the $2\Theta = 89.6^\circ$ line showing deconvolution of the experimental data (empty circles) into two individual bands. Superposition of these bands is also presented.

of diffraction and the Scherrer constant K is conventionally set to 1.0 [27,28]. Using this formula, the mean crystallite size of the synthesized $LaAlO_3$, $La_{0.9}Dy_{0.1}AlO_3$, $La_{0.9}Er_{0.1}AlO_3$ and $La_{0.8}Dy_{0.1}Er_{0.1}AlO_3$ perovskites was calculated from broadening of the (0 1 2) line as 63.4, 54.8, 51.9 and 49.9 nm for $LaAlO_3$, $La_{0.9}Dy_{0.1}AlO_3$, $La_{0.9}Er_{0.1}AlO_3$ and $La_{0.8}Dy_{0.1}Er_{0.1}AlO_3$, respectively.

3.2. TEM studies

TEM micrographs of the $La_{0.9}Er_{0.1}AlO_3$ and $La_{0.9}Dy_{0.1}AlO_3$ samples show that the synthesized powders are composed of spherical-like particles (see Fig. 5(a) and (d)). The distribution of the crystallite sizes is not homogeneous. Fig. 5(c) and (f) shows that the nanoparticles' mean diameter is 49 and 46 nm for $La_{0.9}Er_{0.1}AlO_3$ and $La_{0.9}Dy_{0.1}AlO_3$, respectively. These values are in reasonable agreement with the X-ray results. The high-resolution TEM (HRTEM) images recorded on $La_{0.9}Er_{0.1}AlO_3$ and $La_{0.9}Dy_{0.1}AlO_3$ crystallites show clear lattice fringes (see Fig. 5(b) and (e)). This observation indicates the highly crystalline nature of $La_{0.9}Er_{0.1}AlO_3$ and $La_{0.9}Dy_{0.1}AlO_3$ particles. The lattice fringe spacings in Fig. 5(b) and (e) are about 3.8 and 2.7 Å. These spacings correspond well to the separation between the (0 1 2) and (1 1 0) planes of rhombohedral $LaAlO_3$, respectively.

3.3. Raman and IR spectra

The cubic $Pm\bar{3}m$ unit cell of $LaAlO_3$ comprises of five atoms, which have 15 zone-center degrees of freedom described by irreducible representation of the factor group O_h as $4F_{1u}+F_{2u}$ [29,30]. The F_{2u} mode is silent, one of the F_{1u} modes is acoustic and the remaining three F_{1u} modes are IR-active. Therefore, the cubic phase should show presence of only three IR bands. Transition from the $Pm\bar{3}m$ to $R\bar{3}c$ phase results in doubling of the unit cell and the zone center modes in the $R\bar{3}c$ structure come from modes located at the $\Gamma(0,0,0)$ and $R(1/2,1/2,1/2)$ points of the cubic Brillouin zone [30]. As a result, each of the F_{1u} modes of the cubic phase and the silent F_{2u} mode should split into $A_{2u}+E_u$ and $A_{1u}+E_u$ doublets, respectively [29]. Moreover, new modes should appear from modes located at the $R(1/2,1/2,1/2)$ points of the cubic Brillouin zone and, therefore, the total number of optic modes increases to $A_{1g}+3A_{2g}+4E_g+2A_{1u}+3A_{2u}+5E_u$ [29]. The A_{2g} and A_{1u} modes are silent, A_{1g} and E_g modes are Raman-active and A_{2u} and E_u modes are IR-active. Therefore, there should be eight bands in IR spectra and five in Raman spectra of the $R\bar{3}c$ structure.

Raman spectra of $LaAlO_3$ and $La_{0.9}Dy_{0.1}AlO_3$ are presented in Fig. 6 (Raman spectra of the erbium-containing samples could not be recorded due to very strong luminescence background). Fig. 6 shows that there are three Raman bands below 190 cm^{-1} at 154.2, 126.0 and 36.7 cm^{-1}. Former studies showed that bulk $LaAlO_3$ ($R\bar{3}c$ structure) has a very similar Raman spectrum with the bands at 152–155 cm^{-1} (E_g), 123–125 cm^{-1} (A_{1g}) and 33–34 cm^{-1} (E_g) [6,29,30]. This result is a definite proof that our $LaAlO_3$ nanocrystallites have $R\bar{3}c$ structure. It is here important to add that the 123–125 and 33–34 cm^{-1} modes are soft modes, i.e., they soften to zero wavenumber at the phase transition temperature [31]. Since these bands are observed at very similar wavenumbers both for our nanocrystalline samples and bulk $LaAlO_3$, Raman results indicate that the rhombohedral distortion of the parent cubic structure of nanocrystalline $LaAlO_3$ is similar as that observed for bulk material. In other words, our results do not show any decrease of T_c with decreasing particle size, at least down to about 63 nm, according to our XRD results. This result is consistent with behavior of other perovskite materials, which show significant decrease of T_c usually for crystallites lower than 50 nm [32]. For instance, for $PbTiO_3$ that has the phase transition temperature slightly lower ($T_c=763$ K) than $LaAlO_3$ ($T_c=800$ K), the critical size at which the structure was transformed to cubic was found to be only 9.1 nm [33]. Here it is important to add that the preparation method and the dopant also influence the phase symmetry. For instance, $LaAlO_3$ exhibits the $Pm\bar{3}m$ to $R\bar{3}c$ transition at temperature lower by up to several hundred of K when compared to other $RAlO_3$ perovskites [34,35].

Raman spectrum of $La_{0.9}Dy_{0.1}AlO_3$ also shows presence of three bands, in agreement with the $R\bar{3}c$ structure. However, the Raman spectrum is slightly different from that observed for $LaAlO_3$.

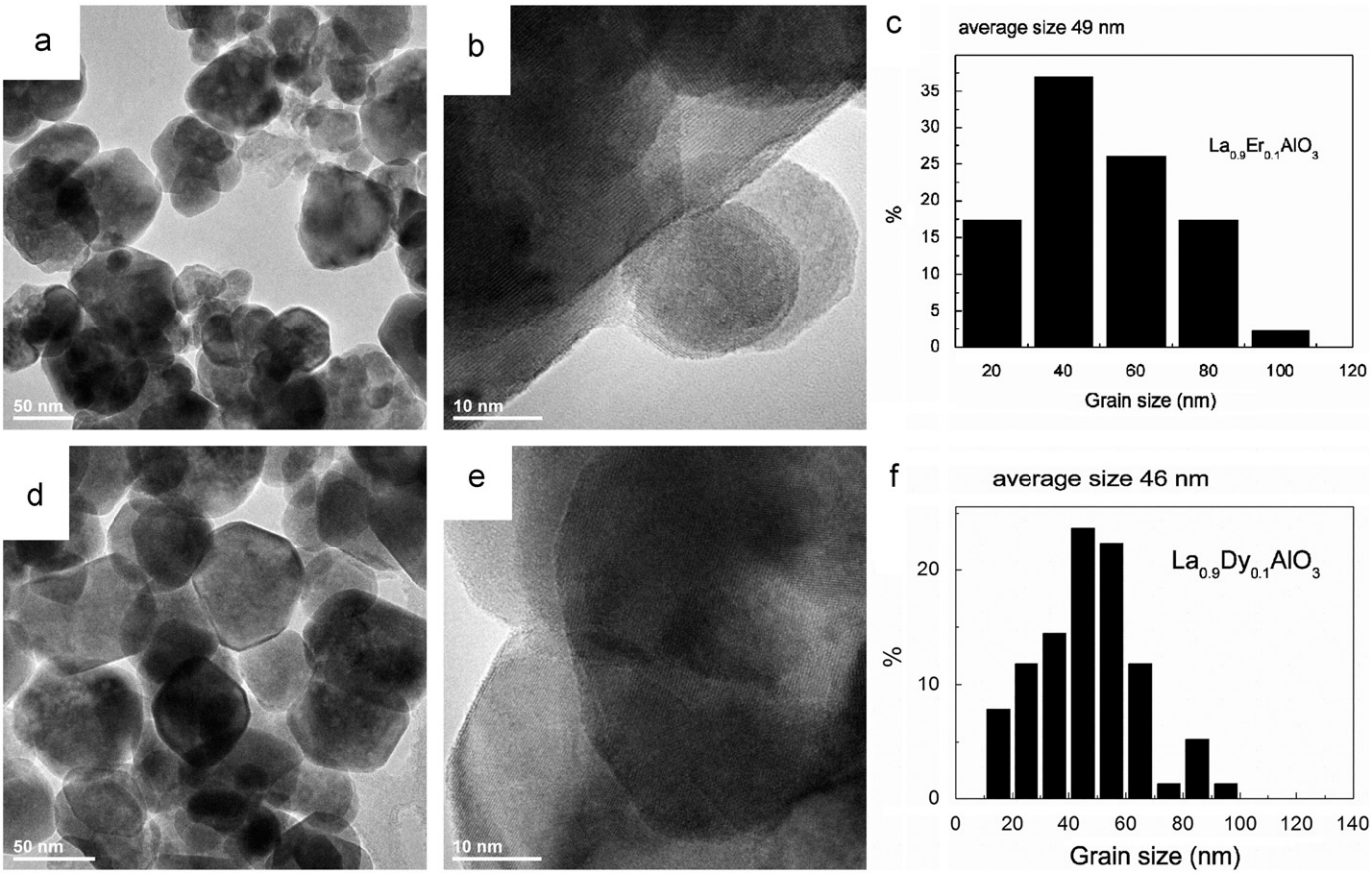

Fig. 5. TEM (a) and (d) and HRTEM images (b) and (e) of $La_{0.9}Er_{0.1}AlO_3$ and $La_{0.9}Dy_{0.1}AlO_3$ particles prepared at 500 °C. The lattice fringe spacings are 3.8 Å and 2.7 Å. The histograms presented in figures (c) and (f) show the particle size distribution.

First, the observed Raman bands are broader. This effect can be attributed to disorder induced by partial replacement of La by Dy atoms. Second, the highest wavenumber mode exhibits weak shift towards higher wavenumbers, i.e., from 154.2 cm^{-1} for $LaAlO_3$ to 155.3 cm^{-1} for $La_{0.9}Dy_{0.1}AlO_3$. In contrast to this behavior, much larger shifts are observed for the remaining modes, i.e., from 126.0 and 36.7 cm^{-1} for $LaAlO_3$ to 135.5 and 39.2 cm^{-1} for $La_{0.9}Dy_{0.1}AlO_3$. Since these modes behave as soft modes, their hardening points to increase in the rhombohedral distortion of $La_{0.9}Dy_{0.1}AlO_3$ when compared to $LaAlO_3$. This behavior can be attributed to smaller ionic radius of Dy^{3+} when compared to La^{3+}. Indeed, former studies showed that in $RAlO_3$ perovskites T_c increases with decreasing size of the rare earth ion [34,35].

IR spectrum of $LaAlO_3$ nanopowders, presented in Fig. 7, shows presence of three doublets at about 696+662, 513+445, 248+200 cm^{-1}. Similar doublets are observed also for $La_{0.9}Dy_{0.1}AlO_3$, $La_{0.9}Er_{0.1}AlO_3$ and $La_{0.8}Dy_{0.1}Er_{0.1}AlO_3$ samples. These doublets have positions close to the three expected IR bands of the cubic phase, which according to the ab initio calculations should be observed at 167, 412 and 648 cm^{-1} [6]. The additional splitting of these bands could be attributed to splitting of the F_{1u} modes of the $Pm\bar{3}m$ structure into $A_{2u}+E_u$ modes of the $R\bar{3}c$ structure. However, lattice dynamics calculations suggest that the separation of the $A_{2u}-E_u$ modes for a given pair should be very small (<11 cm^{-1}) [6,29]. Therefore, Abrashev et al. suggested that although the pair at 692+652 cm^{-1} (696+662 cm^{-1} in our case) can be attributed to the E_u+A_{2u} modes, separation between the modes at 496–525 and 428–460 cm^{-1} (513 and 445 cm^{-1} in our case) is too large to attribute them the E_u+A_{2u} pair [29]. He attributed the higher wavenumber band to the E_u mode arising from the F_{2g} mode located at the $R(1/2,1/2,1/2)$ point of the cubic Brillouin zone and the lower wavenumber band to the E_u+A_{2u} pair [29]. More recent IR reflectivity data are consistent with this conclusion showing that the lower wavenumber band is a doublet with TO values 426.5 and 430.4 cm^{-1} [36]. IR reflectivity data of $LaAlO_3$ single crystal showed only one band in the far-IR region with TO value near 182–184 cm^{-1} [6,29,36]. IR transmission spectra also showed presence of only one broad band but its maximum was shifted to 190–218 cm^{-1} [29]. This band was attributed to the E_u+A_{2u} pair since the theoretical calculations predicted only 7 cm^{-1} separation between these modes [29]. This band corresponds well to the 200 cm^{-1} band of our nanocrystalline $LaAlO_3$.

Let us now discuss the possible origin of the 248 cm^{-1} band, not observed for bulk $LaAlO_3$. First of all it is worth noting that IR spectra of nanocrystalline $LaAlO_3$ in the 400–1000 cm^{-1} region show significant differences when compared to bulk material. First, IR bands of nanocrystalline samples become narrower [11–15]. Second, whereas the band near 496–525 cm^{-1} is weak for bulk $LaAlO_3$ and hardly visible, its intensity strongly increases for nanocrystalline $LaAlO_3$ samples [11–15]. We suppose, therefore, that the band near 248 cm^{-1} can be clearly observed for nanocrystalline samples since its intensity also strongly increases. Moreover, due to linewidth decrease this band can be better resolved from the 200 cm^{-1} band. According to Abrashev et al., the calculated wavenumber of the F_{2u} mode, which is silent in the $Pm\bar{3}m$ structure, is 270 cm^{-1} [29]. Therefore, the additional band at 248 cm^{-1} for our nanocrystalline $LaAlO_3$ sample may be attributed to the E_u mode of the $R\bar{3}c$ structure arising from the F_{2u} silent mode of the $Pm\bar{3}m$ structure.

Although the 696 cm^{-1} (513 and 248 cm^{-1}) bands may be attributed to splitting of the F_{1u} mode into E_u+A_{2u} modes

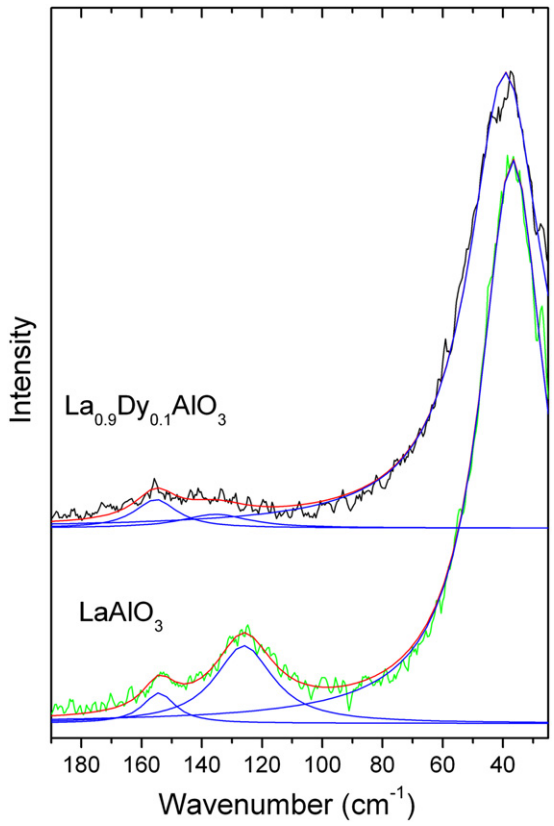

Fig. 6. Raman spectra of $LaAlO_3$ and $La_{0.9}Dy_{0.1}AlO_3$ showing presence of three bands. The figure shows the data (black and green), the fitting (red) and the individual functions obtained from fitting the experimental data to sum of three Lorenzian functions.

(activation of the F_{2g} and F_{2u} modes) due to rhombohedral distortion of the parent cubic structure, an alternative explanation is also possible for these bands. It is well known that shape and maximum intensity of an IR absorption band can be very dependent upon the size and shape of the specimen due to the long-range Coulomb forces [37–41]. For instance, in ionic crystals the surface modes may appear and IR bands may shift to higher wave numbers due to increased polarization charge at the surface of the nanoparticles [37–42]. As a result, the maximum absorption of an IR band may be located between TO and LO. Furthermore, an IR band may even show two maxima. This behavior was, for instance, observed for silicon, which showed maxima near TO and LO values [43]. Change in particle size and morphology may also strongly influence relative intensity of IR bands [44]. The studied here perovskites have the $R\bar{3}c$ structure at room temperature. However, lattice dynamics calculations predict that splitting of the F_{1u} modes into A_{2u} and E_u modes is small ($<11\ cm^{-1}$), i.e. much smaller that the experimentally established LO–TO splitting (93–166 cm^{-1} [36]). Therefore, we assume in our analysis that the rhombohedral distortion can be neglected. In the case of cubic particles dispersed randomly in a medium such as Nujol or KBr, the absorption wavenumbers are related to the bulk crystal TO modes by the relation:

$$\prod_i \frac{\nu_{F_i}^2}{\nu_{T_i}^2} = \frac{[(\varepsilon_0 - 1)g + \varepsilon_m]}{[(\varepsilon_\infty - 1)g + \varepsilon_m]} \quad (1)$$

where ν_{Fi} are the small particle absorption wavenumbers, ν_{Ti} are the bulk crystal TO wavenumbers, ε_0 and ε_∞ are the low-frequency and high-frequency dielectric constants of the crystal, g is the shape factor and ε_m is the dielectric constant of the medium in which the

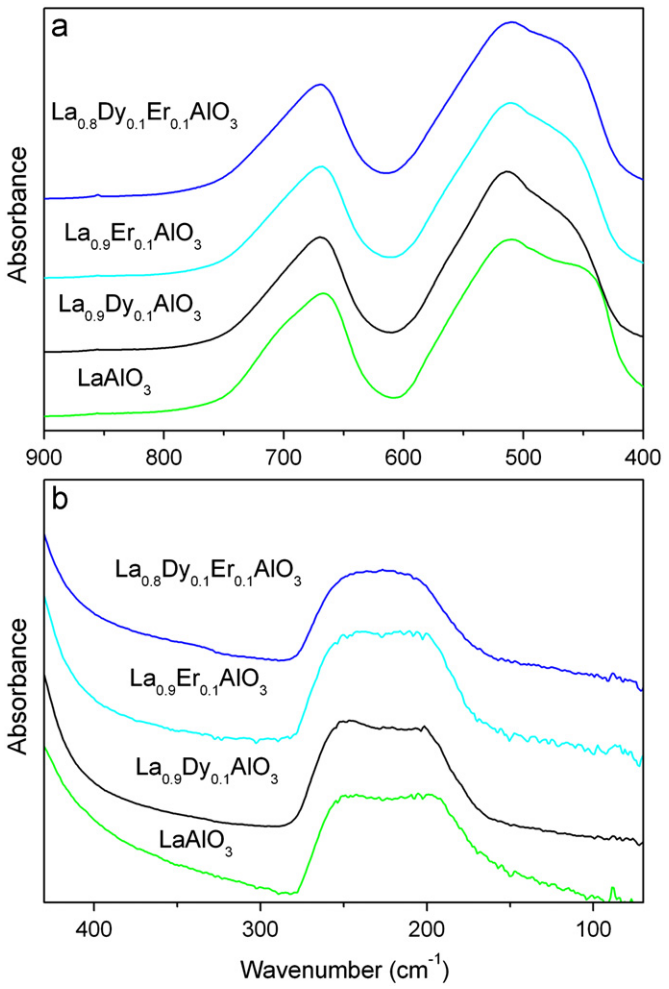

Fig. 7. (a) Mid-IR (in Nujol) and (b) far-IR spectra of $LaAlO_3$, $La_{0.9}Dy_{0.1}AlO_3$, $La_{0.9}Er_{0.1}AlO_3$ and $La_{0.8}Dy_{0.1}Er_{0.1}AlO_3$ samples.

particles are dispersed [41]. For spheres the shape factor g is 1/3 [40,41]. Using Eq. 1 with $g=1/3$, TO values from Ref. 36, $\varepsilon_0=24.1$ [35], $\varepsilon_\infty=4.33$ [2], $\varepsilon_m = 2.33$ for KBr [39] and $\varepsilon_m = 2.15$ for Nujol, we can estimate the absorption wavenumbers of three surface modes as 705, 530 and 237 cm^{-1} (707, 533 and 238 cm^{-1}) in KBr (Nujol). As can be seen, the estimated wavenumbers are close to those observed experimentally. It is therefore likely that the 696, 513 and 248 cm^{-1} bands, not observed for $LaAlO_3$ single crystal, appear in nanocrystalline samples due to surface effects. This assignment is especially likely for the 513 and 248 cm^{-1} bands since they exhibit strong intensity in our samples whereas intensity of the bands arising from the F_{2g} and F_{2u} silent modes of the cubic phase is expected to be rather weak due to weak rhombohedral distortion of the parent phase. Interestingly, whereas literature data show that the band near 496–525 cm^{-1} is always weaker than the 428–460 cm^{-1} band, opposite behavior is observed for our samples. This behavior can be most likely attributed to differences in morphology, degree of agglomeration, surface defects and particle size of our samples and previously studied nanocrystalline $LaAlO_3$. The main factor responsible for this behavior is certainly the crystallization temperature, which was unusually low in our case, i.e. only 500 °C.

3.4. Emission spectra

Dy^{3+} in $LaAlO_3$ host lattice emits light from blue to red region. The luminescence comes from the $^4F_{9/2}$ level of dysprosium.

The most intensive is a yellow greenish emission, which is assigned to the $^4F_{9/2} \rightarrow {}^6H_{13/2}$ transition. There is no difference in the luminescence spectra while excited by different sources like 458 or 355 nm laser lines (see Fig. 8).

The emission of samples doped with erbium (Fig. 9) comes from the $^4S_{3/2}$ to the ground $^4I_{15/2}$ and first excited $^4I_{13/2}$ energy level and also from the neighboring $^2H_{11/2}$ level to the ground state of Er^{3+}.

The cross-relaxation (CR) processes occur in all samples and quench their emission intensity. This is caused by the high concentration of dopant ions, where the probability of an ion pair creation is higher than for the samples with low amount of dopant. Because the non-radiative energy transfers such as CR processes occur in pairs, the concentration quenching is very probable in highly doped samples. The emission of $La_{0.9}Er_{0.1}AlO_3$ is weaker than in $La_{0.9}Dy_{0.1}AlO_3$. This might be due to the fact that Er^{3+} has more intermediate levels in which the cross-relaxation process could occur.

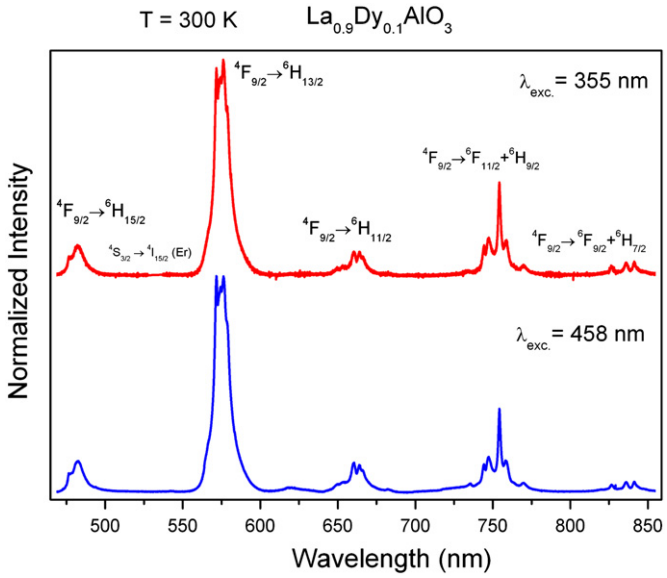

Fig. 8. The emission spectra of $La_{0.9}Dy_{0.1}AlO_3$ excited by the different laser lines.

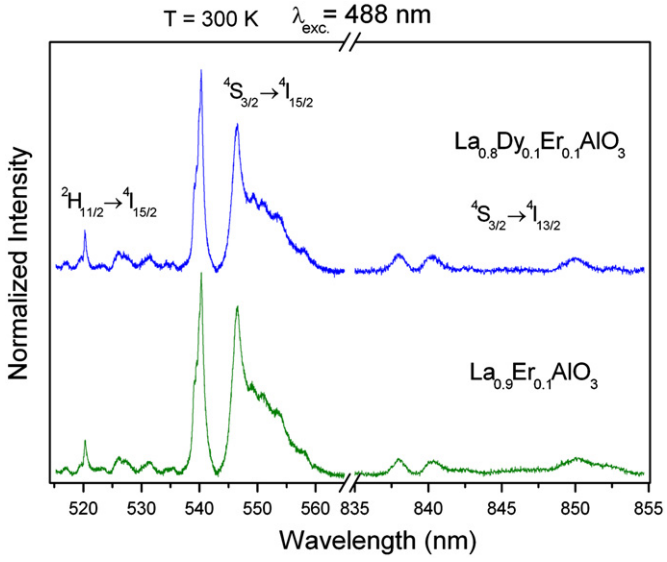

Fig. 9. The emission spectra of $La_{0.9}Er_{0.1}AlO_3$ and $La_{0.8}Dy_{0.1}Er_{0.1}AlO_3$ samples.

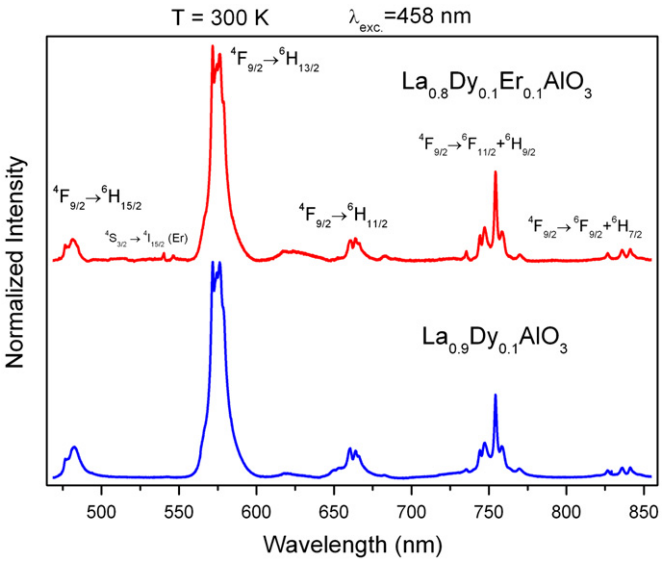

Fig. 10. The emission spectra of $La_{0.9}Dy_{0.1}AlO_3$ and $La_{0.8}Dy_{0.1}Er_{0.1}AlO_3$ samples.

Fig. 10 presents normalized emission spectra of these samples. The emission intensity of $^4F_{9/2} \rightarrow {}^6H_{13/2}$ transition for $La_{0.9}Dy_{0.1}AlO_3$ is more than eight times stronger than this transition in $La_{0.8}Dy_{0.1}Er_{0.1}AlO_3$. This feature could be caused by the non-radiative energy transfer from dysprosium $^4F_{9/2}$ to erbium $^4F_{7/2}$ energy levels, which are close to each other.

4. Conclusions

$LaAlO_3$, $La_{0.9}Dy_{0.1}AlO_3$, $La_{0.9}Er_{0.1}AlO_3$ and $La_{0.8}Dy_{0.1}Er_{0.1}AlO_3$ nanoparticles were synthesized using a novel two-step process, which combines a solid-state metathesis reaction and molten salts synthesis. This synthesis method allows obtaining $LaAlO_3$ nanopowders at remarkably low temperatures, i.e. already at 350 °C although firing at 500 °C is needed in order to get pure phases. This method compares favorably with existing techniques for the synthesis of $LaAlO_3$ powders: i.e., neither La^{3+} and Al^{3+} nitrates nor hydroxides allow obtaining this material as crystalline powders at such low temperatures as those described here. Hence, different attempts carried out to synthesize the target phase by first melting and then dehydrating and firing equimolar mixtures of both hydrated metal nitrates, have shown the onset of crystallinity of the product phase taking place typically in the 800–1000 °C range.

XRD, Raman and IR methods showed that most nanocrystallites in our samples with the mean crystallite size near 50–60 nm have $R\bar{3}c$ structure, the same as bulk $LaAlO_3$. The nanocrystallites with higher symmetry were not detected. IR spectroscopy revealed significant differences between these nanocrystalline samples and bulk $LaAlO_3$. In particular, it showed strong intensity increase of the 513 cm^{-1} band and appearance of a new band near 248 cm^{-1}, not observed for bulk $LaAlO_3$. These features have been attributed to polar nature of the observed modes. Luminescence studied showed that the cross-relaxation processes quench emission intensity of the samples doped with Dy^{3+} and Er^{3+}.

Acknowledgments

This work was partly supported by the Narodowe Centrum Nauki within the project number: N-N507 372335, which is greatly acknowledged.

References

[1] E. Antic-Fidancev, P.J. Deren, J.C. Krupa, J. Alloys Compd. 380 (2004) 376.
[2] P.J. Deren, R. Mahiou, Opt. Mater. 29 (2007) 766.
[3] X. Zheng, L. Zhang, G. Zhao, J. Xu, Y. Hang, H. Pang, M. Jie, C. Yan, X. He, J. Cryst. Growth 271 (2004) 319.
[4] Y.-H. Lu, S. Chi, Opt. Commun. 229 (2004) 317.
[5] J. Kuang, Y. Liu, Chem. Lett. 34 (2005) 598.
[6] P. Delugas, V. Fioretini, A. Filippetti, Phys. Rev. B 71 (2005) 134302.
[7] C.J. Howard, B.J. Kennedy, B.C. Chakoumakos, J. Phys. Condens. Matter 12 (2000) 349.
[8] P.J. Dereń, K. Lemański, A. Gągor, A. Watras, M. Małecka, M. Zawadzki, J. Solid State Chem. 183 (2010) 2095.
[9] R. Pazik, G.A. Seisenbaeva, R.J. Wiglusz, L. Kepinski, V.G. Kessler, Inorg. Chem. 50 (2011) 2966.
[10] P.K. Sahu, S.K. Behera, S.K. Pratihar, S. Bhattacharyya, Ceram. Int. 30 (2004) 1231.
[11] H.F. Yu, Y.M. Guo, J. Alloys Compds. 509 (2011) 1984.
[12] H.F. Yu, Y. Wang, S.S. Wang, Y.M. Kuo, J. Phys. Chem. Solids 70 (2009) 218.
[13] D. Zhou, G. Huang, X. Chen, J. Xu, S. Gong, Mater. Chem. Phys. 84 (2004) 33.
[14] J. Chandradass, K.H. Kim, J. Alloys Compds. 481 (2009) L31.
[15] A.K. Adak, P. Pramanik, Mater. Lett. 30 (1997) 269.
[16] Q. Zhang, F. Saito, J. Am. Ceram. Soc. 83 (2000) 439.
[17] Z. Li, S. Zhang, W.E. Lee, J. Eur. Ceram. Soc. 27 (2007) 3201.
[18] T. Kojima, K. Nomura, Y. Miyazaki, K. Tanimoto, J. Am. Ceram. Soc. 89 (2006) 3610.
[19] P.J. Dereń, K. Lemański, J. Luminesc. 131 (2011) 445.
[20] R.W. Berg, D.H. Kerridge, P.H. Larsen, J. Chem. Eng. Data 51 (2006) 34.
[21] M. Mączka, A.F. Fuentes, L. Kępiński, M.R. Díaz-Guillén, J. Hanuza, Mater. Chem. Phys. 120 (2010) 289.
[22] C.N.R. Rao, B. Prakash, M. Natarajan, Crystal structure transformations in inorganic nitrites, nitrates, and carbonates, The National Standard Reference Data System (NSRDS-NBS 53), National Bureau of Standards, U.S. Department of Commerce, Washington, 1975., p. 48.
[23] R.D. Shannon, Acta Crystallogr. A32 (1976) 751.
[24] M.D. Shaji Kumar, T.M. Srinivasan, C. Subramanian, P. Ramasamy, Ceram. Int. 23 (1997) 419.
[25] R. Elsebrock, C. Makovicka, P. Meuffels, R. Waser, J. Electroceram. 10 (2003) 193.
[26] Powder diffraction diagram simulation program Poudrix V2, Jean Laugier and Bernard Bochu, ENSPG, Grenoble, France, 2001.
[27] S. Chattopadhyay, P. Ayyub, V.R. Palkar, M. Multani, Phys. Rev. B 52 (1995) 13177.
[28] J.M. Amigó, F.J. Serrano, M.A. Kojdecki, J. Bastida, V. Esteve, M.M. Reventós, F. Marti, J. Europ. Cer. Soc. 25 (1995) 1479.
[29] M.V. Abrashev, A.P. Litvinchuk, M.N. Iliev, R.L. Meng, V.N. Popov, V.G. Ivanov, R.A. Chakalov, C. Thomsen, Phys. Rev. B 59 (1999) 4146.
[30] P. Bouvier, J. Kreisel, J. Phys. Condens. Matter 14 (2002) 3981.
[31] S.A. Hayward, F.D. Morrison, S.A.T. Redfern, E.K.H. Salje, J.F. Scott, K.S. Knight, S. Tarantino, A.M. Glazer, V. Shuvaeva, P. Daniel, M. Zhang, M.A. Carpenter, Phys. Rev. B. 72 (2005) 054110.
[32] P. Ayyub, Proc. Indian Nat. Sci. Acad. 67A (2001) 71.
[33] W.L. Zhong, B. Jiang, P.L. Zhang, J.M. Ma, H.M. Cheng, Z.H. Yang, L.X. Li, J. Phys. Condens. Matter 5 (1993) 2619.
[34] T. Basyuk, L. Vasylechko, S. Fadeev, V. Berezovets, D. Trots, R. Niewa, Acta Phys. Pol. 117 (2010) 98.
[35] L. Vasylechko, A. Senyshyn, U. Bismayer, Perovskite-Type Aluminates, Gallates, in: K.A. Gschneidner Jr., J.-C.G. Bünzli, V.K. Pecharsky (Eds.), Handbook on the Physics and Chemistry of Rare Earths, Vol. 39, North-Holland, the Netherlands, 2009, pp. 113–295.
[36] T. Shimada, K. Kakimoto, H. Ohsato, J. Eur. Ceram. Soc. 25 (2005) 2901.
[37] G. Gouadec, P. Colomban, Progr. Cryst. Growth Character. Mater 53 (2007) 1.
[38] I.I. Shaganov, T.S. Perova, V.A. Melnikov, S.A. Dyakov, K. Berwick, J. Phys. Chem. C 114 (2010) 16071.
[39] Q. Zhang, Z. Zhang, Appl. Phys. A 91 (2008) 631.
[40] J.T. Luxon, D.J. Montgomery, R. Summitt, Phys. Rev 188 (1969) 1345.
[41] J.T. Luxon, D.J. Montgomery, R. Summitt, J. Appl. Phys. 41 (1970) 2303.
[42] K. Genzel, T.P. Martin, Phys. Stat. Sol. B 51 (1972) 91.
[43] V.G. Kravets, C. Meier, D. Konjhodzic, A. Lorke, H. Wiggers, J. Appl. Phys. 97 (2005) 084306.
[44] M. Maczka, M. Ptak, M. Kurnatowska, L. Kepinski, P. Tomaszewski, J. Hanuza, J. Solid State Chem. 184 (2011) 2446.